Talanta 299 (2026) 129076

Contents lists available at ScienceDirect

Talanta

journal homepage: www.elsevier.com/locate/talanta

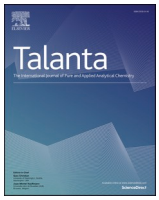

Decoding ancient mortars: complementary strengths of SR-μXRPD and FPA-FTIR in high-resolution binder analysis

Sara Calandra [a,*], Emma Cantisani [b], Barbara Salvadori [b]

[a] Department of Earth Sciences, University of Florence, Florence, 50121, Italy
[b] Institute of Heritage Science, National Research Council of Italy, Sesto Fiorentino, Florence, 50019, Italy

ARTICLE INFO

Keywords:
SR−μXRPD
FPA-FTIR
Ancient mortars
Calcium-carbonate
Silicate

ABSTRACT

The binder of the ancient natural hydraulic mortar is obtained by firing marly or siliceous limestone, which is naturally rich in clay minerals or silica. The setting and hardening process of these mortars is complex, as is their composition, which varies depending on the raw materials, the environment of preservation, and the age of the material. Natural hydraulic mortars from important religious and historic buildings in Florence (i.e. Giotto's Bell Tower, Medici Riccardi Palace and Trebbio Castle) were characterized using conventional techniques (SEM-EDS, TGA, XRPD and ATR-FTIR). In-depth analyses of the binder were performed on the same sample portions through precise sample preparation and the high spatial resolution of advanced techniques, producing high-quality chemical and mineralogical maps. Micro-X-ray powder Diffraction at the European Synchrotron Radiation Facility (SR-μXRPD) and Fourier transform infrared microspectroscopic technique (FPA-FTIR) allow the determination of the distribution and stability of calcium carbonate polymorphs (calcite, aragonite, vaterite) as well as crystalline and amorphous calcium aluminum silicate in the binder of ancient mortars. These results are of fundamental importance for the understanding of ancient production technologies and the chemical transformations that can give these ancient materials their hydraulic behavior.

For the first time, SR-μXRPD and FPA-FTIR have been used to study ancient natural hydraulic mortars, demonstrating the complementarity of these high-resolution techniques for mapping compounds in the historic binders.

1. Introduction

Mortars are heterogeneous materials consisting of binders, aggregates and possible organic/inorganic additives. They have been used for various purposes since antiquity until today, e.g. as bedding for stone and bricks, as plaster for walls, as filling material for masonries [1]. Excluding clays and gypsum, air hardening (or aerial) and hydraulic limes are the most historically diffused types of binder. In aerial mortars the $Ca(OH)_2$, formed by slaking of CaO, produced by burning almost pure calcium carbonate rocks, reacts with the CO_2 present in the air, forming a cohesive material, named anthropogenic calcite. Historically, calcium and magnesium lime binders are used, depending on the composition of the limestone selected for lime production. Hydraulic mortars, on the other hand, set and harden under special conditions, such as high humidity or even under water. Ancient hydraulic mortars were made using natural hydraulic lime binders (so-called natural hydraulic mortar) or mixing air hardening binders with pozzolanic materials (i.e. pozzolana mortar). The modern hydraulic binders (hydraulic lime, formulated lime, cement) are produced industrially at higher temperatures and with specific raw materials. Setting takes place through a hydration reaction between water, calcium silicates and calcium aluminates [2–5]. Historical hydraulic mortars were obtained by firing marly/siliceous limestones to obtain a natural hydraulic binder or by addition of hydraulic components (volcanic ash, pozzolanic materials, forging scoriae, crushed ceramics) to air-hardening to obtain a "pozzolanic" binder. The hardening process consists of the carbonation of calcium hydroxide and the hydration of calcium silicates and calcium aluminates. While pozzolanic mortars were widely used in the Roman period [5,6], natural hydraulic mortars were less common until the XIX and early XX centuries, when a special type of hydraulic binder was developed that fired impure, clayey limestones for the production of so-called ''Roman cements'' [7,8]. In Tuscany (Italy), a natural

This article is part of a special issue entitled: Cultural Heritage Analysis published in Talanta.

* Corresponding author.
E-mail addresses: sara.calandra@unifi.it (S. Calandra), emma.cantisani@cnr.it (E. Cantisani), barbara.salvadori@cnr.it (B. Salvadori).

https://doi.org/10.1016/j.talanta.2025.129076
Received 6 May 2025; Received in revised form 2 October 2025; Accepted 2 November 2025
Available online 4 November 2025

hydraulic lime binder obtained by burning a marly limestone known as Pietra Alberese (Monte Morello Formation) has been used since the Middle Ages [9,10]. Numerous analytical techniques are used to evaluate the composition of each of these components and to analyse the new phases that develop during the setting and hardening of historical hydraulic mortars [11–14].

Our research focuses on analysing the binder of natural hydraulic mortars obtained by firing marly limestone, which is naturally rich in clay minerals. After setting, the phases of non-hydrated clinker, calcite, calcium-modified silica gel and aluminum oxide stabilize (resulting from the presence of non-hydrated clinker, calcium silicate hydrates CSH, calcium silico-aluminate hydrates CASH, and calcium aluminate hydrates CAH) [2,15,16] in natural hydraulic binders. In addition to calcite, aragonite and vaterite are also commonly found. The carbonation of $Ca(OH)_2$ has as its first step the transformation into amorphous calcium carbonate (ACC), then it is transformed into aragonite (arg), vaterite (vtr) or calcite (cal) [17–19]. This transformation usually proceeds sequentially ACC-arg-vtr-cal without external influences. The ACC is unstable and crystallizes into $CaCO_3$ (arg, vtr or cal), with calcite being the most stable form [20,21].

The basic factors affecting the crystallization of $CaCO_3$ polymorphs are temperature, pH, chemical binder composition. There are many hypotheses about their formation. In Black et al. [22], it is shown that CSH and CAH phases form imperfect or very fine crystals, favouring the formation of vaterite and aragonite. However, in other studies [7], it has been shown that both vaterite and aragonite are precursors during the carbonation of portlandite ($Ca(OH)_2$, CH). One possible factor that favors the crystallization of metastable polymorphs is the mortar maturation conditions in a low CO_2 environment [23]. According to some authors, the formation of aragonite and vaterite can be promoted by the addition of an organic compound during mortar mixing [24,25]. The presence of $Ca(OH)_2$ ensures a pH $>$ 12 in fresh mortar, and thus favourable conditions for carbonate crystallization in the form of calcite. After carbonation, a decrease in the pH of the environment is observed, an optimal condition for the formation of vaterite and aragonite [26]. In Seymour et al. [6], it is mentioned that vaterite is formed in pozzolanic mortars by the modification of CASH. In the post-pozzolanic process, the unreacted ceramic fragments continue to dissolve over time, leading to the formation of CASH and vaterite.

In this framework, the identification of composition and distribution of these compounds in ancient hydraulic natural binders can shed light on their formation process. To better understand the processes and phases involved, it is crucial to use analytical techniques with high lateral resolution that are able to distinguish between amorphous and crystalline phases.

Fourier Transform Infrared spectroscopy (FTIR) allows the detection of the molecular composition of both amorphous and crystalline materials. In recent decades, advancements in solid-state array detectors have revolutionized molecular spectroscopy enabling chemical imaging, with the development of instruments equipped with Focal Plane Array (FPA) detectors which provide the highest sensitivity and spatial resolution in molecular imaging to be achieved in a short time. Chemical imaging generates a chemical map of the sample or system under investigation, containing spectral information and displaying the chemical distribution of components. The ability of FPA-FTIR microscopy to generate highly spatially resolved maps has been exploited in fields, such as biochemistry, biomedicine and earth sciences [27,28]. Moreover, its application in Heritage Science is attracting growing interest, as reflected in the increasing number of studies in the literature. While FPA-FTIR is used in ATR mode for chemical imaging of multi-layered painted artworks [29–31], its potential for analyzing heterogeneous materials, such as mortars, makes it particularly valuable for understanding complex historical materials and their composition. This approach allows for the identification of the chemical distribution across different areas of a sample, including portions of the binder or lumps.

At the same time, access to synchrotron radiation facilities for the study of ancient materials has increased in recent years. X-ray based techniques such as X-ray fluorescence (SR-μXRF), X-ray powder diffraction (XRPD), and X-ray absorption spectroscopy (SR-XAS) offer the advantage of high sensitivity, sub-micron resolution and mapping capabilities, making them powerful tools for investigating elements and mineralogical phases in heterogeneous and multilayered materials [32–35]. In this context, we exploit high-resolution micro-X-ray powder diffraction at the European Synchrotron Radiation Facility (SR-μXRPD) to generate spatially resolved crystalline phase maps of ancient mortars.

For the first time, this study explored the possibility to map the distribution of amorphous and crystalline phases in the same areas of ancient natural hydraulic mortars by combining high-resolution SR-μXRPD and FPA-FTIR techniques.

After a preliminary characterization with traditional X-ray powder diffraction (XRPD) and Attenuated Total Reflectance-Fourier Transform Infrared Spectroscopy (ATR-FTIR), mortar samples from historical buildings in Florence (Italy) [13,36] were analysed with SR-μXRPD and FPA-FTIR to map the phases of non-hydrated clinker, calcium carbonate polymorphs and calcium-modified silica gel in binder and lumps. Lumps can be referred to unmixed portions of binder.

The SR-μXRPD analysis conducted at beamline ID13 within the framework of the "Historical Materials BAG: A New Facilitated Access to Synchrotron X-ray Diffraction Analyses for Cultural Heritage Materials at the European Synchrotron Radiation Facility (ESRF)" [32] allowed us to distinguish different chemical species, based on their distinct diffraction patterns. Additionally, it enabled precise mapping of crystalline compounds with high spatial resolution over large areas of thin sections. In the same areas, chemical imaging with FPA-FTIR technique was performed for the detection of both crystalline and amorphous phases, exploiting the reflectance mode.

2. Materials and methods

Mortars belonging to religious and historic buildings in Florence were investigated (Table 1). They consist of a natural hydraulic binder mixed with silicate and carbonate sand. The weak hydraulic characteristics are due to the use of a marly limestone for the production of binder, as demonstrated in previous papers [36,37]. The firing of this marly limestone determines formation of carbonate polymorphs as calcite, aragonite and vaterite and the development of CASH phases [7].

2.1. Sample selection and preliminary characterization

From three thoroughly investigated case studies, mortar samples with natural hydraulic binder were collected and analysed.

The binder and lump area of the historical mortar samples were identified with the aid of the stereomicroscope (Fig. 1a–c). Before cutting, a small amount of powder (labeled as Pn) was taken from the mortar samples to perform ATR-FTIR and XRPD analysis (Table 1).

Table 1
Summary of analysed mortar samples from historical Florentine buildings, including sample descriptions, hydraulicity behavior (HI index), and the specific samples Pn (powder) and Sn (thin section) selected for preliminary characterization.

ID	Description of sample	HI index	Analysed fractions
A	In-fill mortar from foundation of Giotto's Bell Tower	0.18 ± 0.07	P1, P2, P3 and P4, S1, S2
B	Bedding mortar from external wall of Trebbio Castle Tower	0.19 ± 0.08	P1, P2 and S1, S2
C	*Nucleus* mortar from internal masonry of Medici Riccardi Palace	n.d.	P1, and S1, S2

The average HI index was obtained via SEM-EDS and TGA analyses in previous studies (for details on samples characterization [36,37]. SEM-EDS analysis of the binder and lime lumps revealed that the maximum MgO content is 1.4 % wt for Case A, 0.4 % wt for Case B, and 1.3 % wt for Case C.

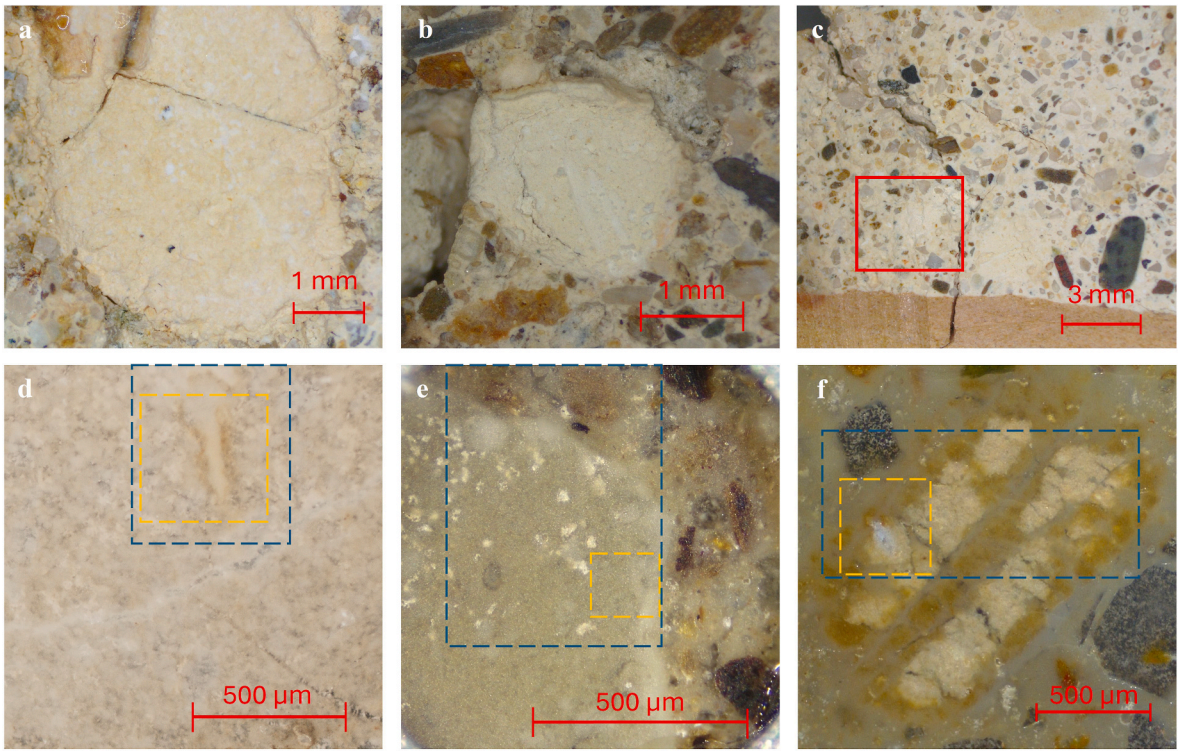

Fig. 1. Stereomicroscope images of historical mortar samples showing binder and lump areas selected for analysis: a) Case A: Giotto's Bell Tower; b) Case B: Trebbio Castle; c) Case C: Medici Riccardi Palace. Optical microscope images (4–10 × magnification) of the thin sections: d) Case A: Giotto's Bell Tower, lump area; e) Case B: Trebbio Castle, lump and binder areas; f) Case C: Medici Riccardi Palace, lump and binder areas. Yellow squares in all the images refer to SR-µXRPD measurements, while blue squares refer to FPA-FTIR analyses. (For interpretation of the references to colour in this figure legend, the reader is referred to the Web version of this article.)

A Philips X'Pert PRO X-ray powder diffractometer (XRPD) with a Cu anticathode (wavelength $\lambda = 1.54$ Å) was used to analyse powders. The instrument operated at a current intensity of 30 mA and a voltage of 40 kV. The 2θ range explored was between 3 and 70° with a step size of 0.02°. The X'Pert HighScore program and the ICCD database were utilised to identify the crystalline phases.

In addition, a FTIR ALPHA Bruker was used with an ATR system. The spectra obtained from the analysis of the powdered sample were acquired and processed using OPUS 7.2 software (Bruker Optics GmbH, Ettlingen, Germany) and Spectragryph 1.2.15 (SpectraGryph; Optical spectroscopy software; www.effemm2.de/spectragryph), respectively. The acquisition was carried out in the spectral range between 4000 and 400 cm^{-1}, with a resolution of 4 cm^{-1} for 24 scans.

2.2. Sample preparation and advanced techniques

Polished thin sections of the analysed historical mortar samples with a thickness of 50 µm [38], mounted on a polycarbonate base, were prepared and labeled as Sn (Table 1).

The same areas in the thin sections were analysed using advanced techniques (SR-µXRPD mapping and FPA-FTIR mapping). The advantages of the chosen sample preparation method for each technique are described in detail below.

SR-µXRPD mapping was performed at the SR-µXRPD branch of the ID13 beamline of the European Synchrotron Radiation Facility (ESRF, Grenoble) thanks to the BAG Historical Materials (proposal HG-172) [32]. The sample preparation method used for SR-µXRPD mapping offers significant advantages as it minimizes the interference from the support material during diffraction analysis. By polishing the thin sections to 50 µm thickness and mounting them on a polycarbonate support, contributions from the support to the diffraction signal were effectively avoided.

This approach also enables a detailed spatial resolution of the crystalline phases within the heterogeneous matrix, and thus the differentiation of finer minerals. In addition, the preparation preserved the integrity of the porous structure and ensured that the inherent heterogeneity of the mortar was preserved and could be effectively analysed.

To perform raster scan maps, a beam size of approximately 2 × 2 µm was used with a step size of 1 µm in x and y directions, with an acquisition time per point of 10 ms at 13.0 keV and a flux of 2.0 × 1011 ph s^{-1} (at I = 34 mA electron beam current). The two-dimensional diffraction patterns collected in transmission have been azimuthally integrated using dedicated Jupyter notebooks, based on the PyFAI software package13 and were then analysed with PyMCA software by the BLISS (Beam Line Instrumentation Software Support) group of the ESRF. This software can be downloaded for free and facilitates the interactive and batch processing of large data sets, making it particularly well-suited to X-ray imaging. The identification of the crystalline compounds was performed with the ICCD database.

FPA-FTIR analyses were performed on the same areas using a Bruker LUMOS II FTIR microscope (Bruker Optics GmbH, Ettlingen, Germany) equipped with a liquid-N_2 cooled 32x32 element Focal Plane Array (FPA) detector. The measurement acquisition modes with FPA-FTIR include external reflection, ATR, and transmission. The choice of acquisition mode depends on the type of sample, nature and quantity of available samples, and research questions [31]. The transmission mode is unsuitable on thin sections, due to the presence of polycarbonate support which would be detected, making the spectrum rather complex and possibly hiding bands of interest. As far as external reflection is concerned, the roughness and porosity of the mortar samples may cause uninterpretable distortions in the spectrum, even in cross section. On the other hand, the samples under investigation contain aggregate portions with hardness comparable to that of the germanium instrument crystal [39], making ATR mode not recommended. Taking these critical issues

into account, we chose to adopt the external reflection mode, ensuring the use of highly polished thin sections. Indeed, polishing improves FTIR reflection by enhancing specular reflection and reducing scattering, leading to higher signal quality and more accurate identification of absorption features. This approach is essential for obtaining high resolution, high quality chemical images, particularly when dealing with the irregular and porous surfaces characteristic of mortars.

FPA-FTIR images were acquired in reflection mode within a 4000–750 cm^{-1} spectral region, each as a single FTIR image (1024 spectra) covering a sampling area of ca. 150 × 150 μm^2, with resolution 4 cm^{-1} and 128 scans. In reflection mode, a single spectrum in each FTIR image represents molecular information acquired from ca. 5 × 5 μm^2 area on the sample plane. Background measurements were taken prior to sample spectral images, on a gold mirror. The collected FTIR spectra were processed using OPUS 8.2 software (Bruker Optik GmbH, Ettlingen, Germany). Fig. 1d–f shows the SR-μXRPD and FPA-FTIR investigated areas.

3. Results

3.1. Preliminary results using XRPD and ATR-FTIR

XRPD analysis (Table 2) of the powders taken from the samples before the preparation of the thin section revealed the presence of: aragonite (d 3.39 Å - 26.23° 2θ, PDF 41–1475), calcite (d 3.04 Å - 29.40° 2θ, PDF 5–586), vaterite (d 2.73 Å - 32.78° 2θ, PDF 33–26), CASH/CAH (identify as: d 6.25 Å - 14.16° 2θ and d 7.58 Å - 11.65° 2θ [40]), portlandite (d 2.63 Å - 34.09° 2θ, PDF 44–1481). The presence of quartz (d 3.34 Å - 26.65° 2θ) refers to contamination from aggregate.

The same powders were analysed on FTIR. In the FTIR spectra (in Fig. 2, an example of A_P1-3 samples), a strong and broad band is evident around 1450 cm^{-1} with an extended shape, attributed to the overlap of the main asymmetric $\nu_3(CO_3)$ vibrations at 1420 cm^{-1} for calcite, at 1475 cm^{-1} for aragonite, at 1490 cm^{-1} for vaterite; the band at 874 cm^{-1} typical of asymmetric $\nu_2(CO_3)$ vibrations in calcite and vaterite is also visible, as well as the band at 856 cm^{-1} related to aragonite [41,42]. Finally, the vibration at 712 cm^{-1} is present, characteristic of both calcite and aragonite, which also exhibits the adjacent peak at 700 cm^{-1}.

Moreover, the presence of silicates is evident from the poorly resolved peak at 1041 cm^{-1} [43,44]. Neither the weak vibrations of vaterite at 1085 cm^{-1} and 1070 cm^{-1}, nor the stronger ones at 970 cm^{-1} are identifiable due to the interference of silicates. These compounds belong to amorphous phases of natural hydraulic binder [45] which produce broad and intense peaks that conceal the characteristic vibrations of vaterite. ATR-FTIR analysis does not detect the presence of organic phases. The co-presence of polymorphs of calcium carbonate and silicate bands makes it difficult to distinguish the characteristic bands of vaterite (since the peak at 744 cm^{-1} is absent), while distinctive peaks can be observed for calcite and aragonite. However, the characteristic peaks of vaterite are shown in Fig. 2.

Table 2
XRPD results of binder-rich portions.

ID sample	Vtr	Cal	Arg	Other
A_P1	++	++	–	CASH/CAH (++)
A_P2	+++	++	++	–
A_P3	+++	++	++	–
A_P4	+	++	–	–
B_P1	–	++	+	–
B_P2	–	++	*	Quartz (*)
C_P1	*	+	*	Portlandite (++), CASH/CAH (*)
C_P2	–	++	+	Portlandite (+), quartz (*)

Vtr: vaterite; Cal: calcite; Arg: aragonite; CASH: calcium silico-aluminate hydrates; CAH: calcium aluminate hydrates [19]. +++: very abundant; ++: abundant; +: present; *: traces; -: below detection limit.

3.2. Advanced technique results

The mapping performed with ID13 allowed the evaluation of the distribution of crystalline calcium carbonate polymorphs and CASH phases. From the SR-μXRPD results, the main peaks of the mineralogical phases under investigation are clearly distinguishable, as previously highlighted in the XRPD analysis section. The high resolution of SR-μXRPD allows us to assess the presence of crystalline CASH phases, enabling a more in-depth analysis of the constituent mineralogical phases.

The distribution of calcite, aragonite and silicate phases (quartz, amorphous silicates and calcium silicate) was also well determined with FPA-FTIR.

The spatial distribution of carbonate and silicate components was highlighted with chemical imaging using FPA-FTIR, exploiting the most characteristic bands for each compound.

- Case A: Giotto's Bell Tower

The spatial distribution of components on enriched-portion of binder (lump in Fig. 3a) was highlighted with chemical imaging using FPA-FTIR, exploiting the most characteristic bands mentioned above: 860 cm^{-1} for aragonite, 878 cm^{-1} for calcite/vaterite, and about 1000 cm^{-1} for silicate (spectra analysis point in Fig. 3).

The FPA-FTIR map shows the distribution of aragonite (867–844 cm^{-1}), calcite/vaterite (884–867 cm^{-1}) and silicates (1147–974 cm^{-1}) (Fig. 3a).

Based on the analysed bands, the identified silicate is not quartz associated with the aggregate, but neoformed silicates related to natural hydraulic binder [23,36,45].

An important result is that no aragonite is found in areas where calcite/vaterite occurs and *vice versa*; only in the transition zones are both compounds observed. The region studied to create the map does not allow vaterite to be distinguished from calcite. Silicates are widespread and concentrated in areas where significant amounts of calcite/vaterite are present. Furthermore, FPA-FTIR analysis does not detect the presence of organic phases, as is the case with ATR-FTIR.

The SR-μXRPD maps of the sample are shown in Fig. 3b. The $CaCO_3$ polymorphs: aragonite, calcite and vaterite were identified with CASH.

The CASH phase can be identified as gismondine structure (d 2.71 Å - 33.03° 2θ, d 4.25 Å - 20.88° 2θ, d 3.19 Å - 27.95° 2θ; PDF 39–1373). This phase has been observed in cementitious materials, such as stratlingite or kaoite [46,47].

It is worth noting that the distribution of aragonite, calcite and silicate phases is similar to that found by FPA-FTIR analyses, confirming the complementarity of the two techniques. Vaterite is concentrated in the central area, identified with FPA-FTIR in the range 884–867 cm^{-1}. Compared to FPA-FTIR, the SR-μXRPD technique makes it possible to distinguish areas consisting of vaterite and calcite. The point where the vaterite content is higher corresponds to a higher amount of CASH and is surrounded by calcite and aragonite. The CASH phase is more diffuse and follows the distribution of silicate detected in the FPA-FTIR. Analysing IR vibrations of silicates, peak broadening may indicate a lower internal order of the material [44,48]. Given the presence of gismondines in SR-μXRPD, one can assume the presence of both amorphous and crystalline silicates.

- Case B: Trebbio Castle

FPA-FTIR chemical imaging and the spectra collected to perform imaging are reported in Fig. 4a (calcite, aragonite and silicates and respectively bands). The FPA-FTIR map shows the distribution of aragonite (867–844 cm^{-1}), calcite (884–867 cm^{-1}) and silicate phases (1147–974 cm^{-1}), and quartz (819-761 cm^{-1}) in the lump and binder areas.

Aragonite is widely distributed in the map in both lump and binder.

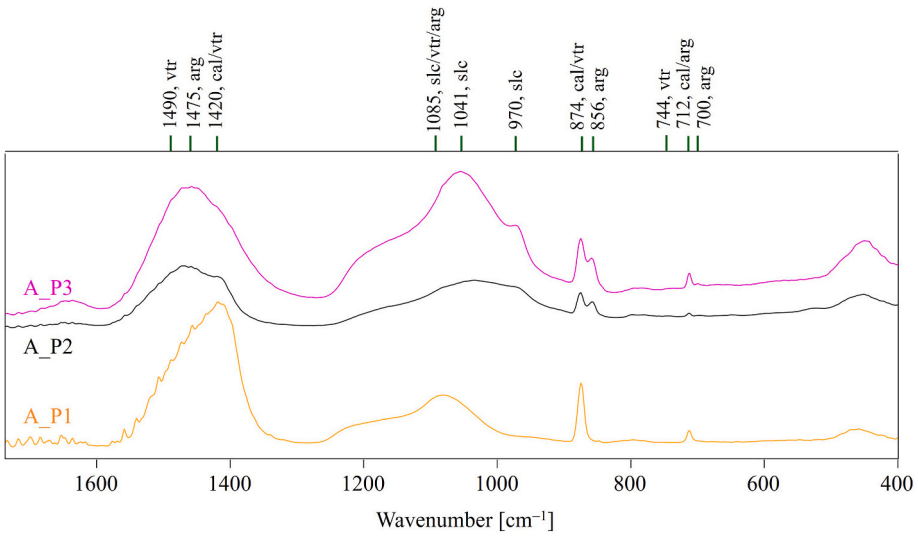

Fig. 2. ATR-FTIR analyses of A_P1, 2 and 3 samples. Calcite (cal), vaterite (vtr), aragonite (arg), and silicate (slc) are observed in the pink and black spectrum. Calcite, silicate and/or vaterite present in orange spectra. A guide to the peak positions is depicted in the spectrum above. (For interpretation of the references to colour in this figure legend, the reader is referred to the Web version of this article.)

Calcite is present in the intermediate zone between binder and lump, correspondingly in areas with low aragonite content. In the areas where both phases (Arg and Cal) are present, the presence of silicates is also evident (pink and black spectra, Fig. 4a). No silicate bands are observed in the calcite-rich zone (green spectrum, Fig. 4a).

Silicates are quite present and concentrated in the binder zone. The presence of quartz (the most characteristic bands in the range 819–761 cm^{-1}, red spectrum in Fig. 4a) can be referred to the mortar aggregate.

Compared to the previous sample, the intensities of the peaks are lower and less well resolved; this is probably due to the higher porosity of the sample.

The SR-μXRPD maps of the binder and the lump are shown in Fig. 4b. Aragonite and calcite were identified and mapped, while vaterite is not present.

The SR-μXRPD results are consistent with the FPA-FTIR results and show a higher concentration of calcite in the same area highlighted in the FPA-FTIR maps. Aragonite is less strongly represented. No crystalline silicate phases attributable to CASH or CAH compounds are observed. So, the silicate phases identified in FPA-FTIR are partially composed of amorphous phases.

- Case C: Medici Riccardi Palace

FPA-FTIR chemical imaging and the spectra collected to perform imaging are reported in Fig. 5a (calcite, aragonite and silicates and its respective bands, including quartz). The FPA-FTIR map shows the distribution of aragonite, calcite, silicates, and quartz in the lump and binder areas.

Aragonite is rare on the map both in lumps and in the binder, while calcite seems to be widespread. In general, aragonite occurs together with calcite in most areas. This is confirmed by the pink and blue spectra (Fig. 5a), in which the two polymorphic phases of $CaCO_3$ are found together with silicates. No other bands are observed in the calcite-rich zones (green spectrum, Fig. 5a).

Silicates are mainly found in the lump and associated with the presence of aragonite. In the silicate region, in addition to the typical band at 1035 cm^{-1}, bands at 903 and 965 cm^{-1} were also observed. These bands are due to the vibrations of chain silicates and reflect a structural configuration with asymmetrically bonded oxygen atoms between silicon tetrahedra [49]. In mortars, this band may indicate the presence of chain silicates or chemical modifications with bridging and non-bridging oxygen compounds during hydration and curing. Chain silicates are mainly observed in the lump region [50].

Analysis of the silicate spectra also reveals the presence of quartz due to impurities from aggregate.

Fig. 5b shows the SR-μXRPD maps of a small area between the lump and the binder. Aragonite, calcite, vaterite, portlandite and CASH/CAH are identified and mapped. Calcite is diffuse in both the binder and the lump, while aragonite is more concentrated in the edge of the lump and less widespread in the binder. The coexistence of calcite and aragonite is observed in several areas, which is consistent with the results of the FPA-FTIR analysis. Portlandite is widespread, which is more abundant in the lump area, but cannot be detected in the chemical analysis. The diffraction peak observed at 32.17° 2θ could be primarily due to the presence of hydrocalumite ($Ca_4Al_2(OH)_{12}Cl–6H_2O$), a common secondary phase in historical mortars. Hydrocalumite exhibits a strong reflection near this angular position, which agrees well with the conventional experimental data. Alternatively, other CASH or not hydrated phases (CAS) may also contribute to the observed peak. Gehlenite ($Ca_2Al_2SiO_7$) in particular shows a reflection around 32.3° 2θ, and its formation is plausible given the marly nature of the original limestone and the firing conditions typical of historic lime production. Based on this peak, the CASH/CAH/CAS map was identified.

Analysing IR vibrations of silicates, given the presence of silicate phases in SR-μXRPD, the distribution is similar and one can assume the presence of both amorphous and crystalline silicates.

4. Discussion

The presence of metastable $CaCO_3$ polymorphs and hydraulic calcium silicate–aluminate phases in ancient mortars can be interpreted in terms of the complex variables that control the production of natural hydraulic lime (NHL). Starting from the same marly/siliceous limestone, with similar chemical and mineralogical composition and textural features, used for the production of natural hydraulic lime the presence of both metastable $CaCO_3$ polymorphs and hydraulic calcium silicate–aluminate phases can be determined at different stages of mortar production: during calcination of the limestone, slaking of quicklime, and subsequent setting and hardening of the binder. Each step introduces specific variables that strongly influence the compounds eventually preserved in archaeological mortars [51,52].

During calcination, the decomposition of calcite and the formation of reactive silicate and calcium aluminate phases depend on maximum kiln temperature, residence time, and the partial pressure of CO_2 [53].

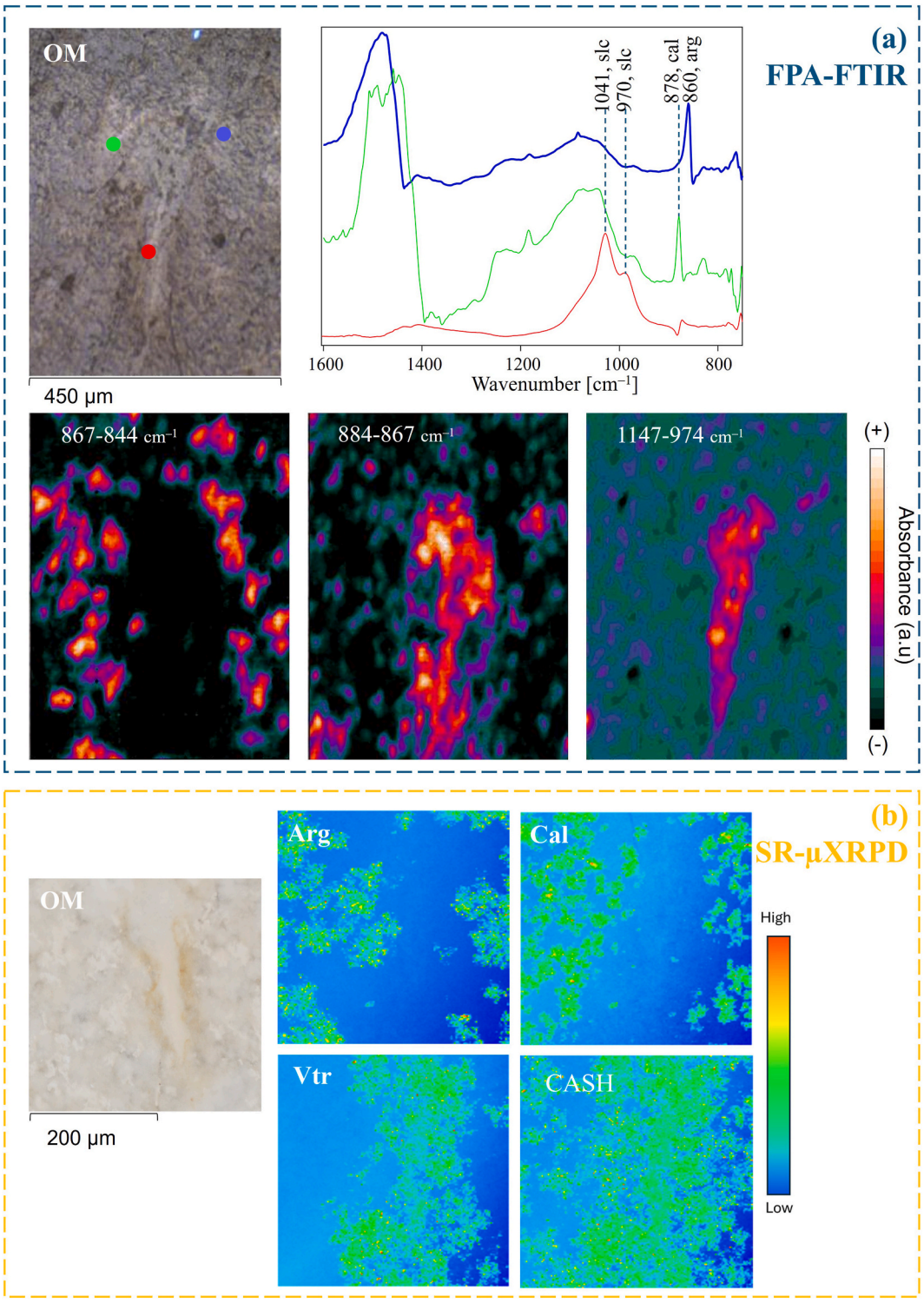

Fig. 3. Analysis of lump with FPA-FTIR and SR-μXRPD. a) FPA-FTIR: Investigated area using OM (ROI ~450 × 600 μm^2), point analysis, and absorbance spectra. Chemical distribution maps: aragonite (867–844 cm^{-1}), calcite/vaterite (884–867 cm^{-1}), silicate (1147–974 cm^{-1}). b) SR-μXRPD: Investigated area using OM (ROI ~400 × 360 μm^2) and distribution maps: Arg, cal, vtr, and CASH. Maps presented in a colourmap ranging from low to high values of relative intensity: from black to white in FPA-FTIR maps and from blue to red in SR-μXRPD maps. (For interpretation of the references to colour in this figure legend, the reader is referred to the Web version of this article.)

Heterogeneous temperature distributions within traditional kilns may lead to incomplete decomposition of calcite in low-temperature zones (600–900 °C) [54], while localized hot spots promote the formation of high-temperature silicate and calcium aluminate phases. These factors not only determine the assemblage of Ca-silicates and aluminates, but also influence the long-term setting behavior of NHL mortars and their mechanical performance [9,10,13,14,55].

In the slaking process, additional transformations take place. The reactivity of CaO with water is affected by raw material features (composition, particle size, porosity) [16,56–58], calcination

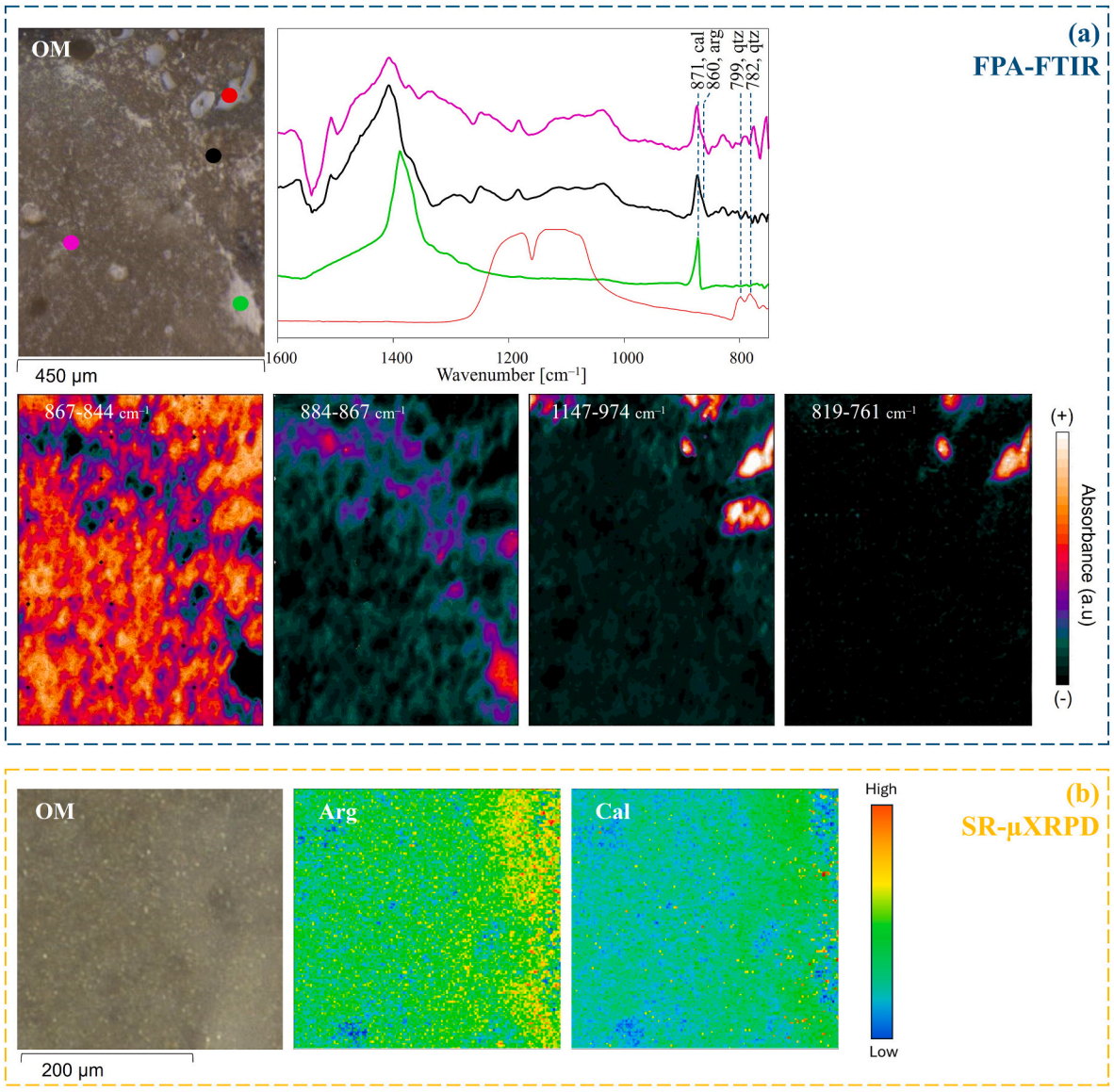

Fig. 4. Analysis of lump and binder with FPA-FTIR and SR-μXRPD. a) FPA-FTIR: Investigated area using OM (ROI ~450 × 600 μm^2), point analysis, and absorbance spectra. Chemical distribution maps: aragonite (867–844 cm^{-1}), calcite (884–867 cm^{-1}), silicate (1147–974 cm^{-1}) and quartz (819-761 cm^{-1}). b) SR-μXRPD: Investigated area using OM (ROI ~300 × 280 μm^2) and distribution maps: arg and cal.

conditions, storage time, the method of slaking and agitation, and the composition of slaking water [57]. Potgieter et al. [58] demonstrated that air exposure prior to slaking reduces quicklime reactivity due to the formation of superficial $Ca(OH)_2$ and/or $CaCO_3$ layers. Mineralogical analyses further show that slaking reduces the abundance of primary hydraulic phases relative to calcined precursors, while promoting the formation of hydrated calcium aluminates (hydrogarnet, Ca-AFm) and increasing the amorphous fraction, likely linked to poorly ordered CSH [16,57–59]. Exposure to CO_2 during slaking additionally explains the partial carbonation of portlandite into calcite and aragonite, the latter favored by the high temperatures reached in this process. Such evidence confirms that the coexistence of carbonates and CASH phases may originate already during slaking, influencing the subsequent stabilization of metastable polymorphs.

Finally, during setting and hardening processes, laboratory-produced NHLs typically exhibit calcite, portlandite (ordered and disordered), crystalline calcium silicates (C_2S, belite and C_3S, alite), calcium aluminates (C_3A, Celite), quartz, and amorphous phases [16]. In contrast, archaeological mortars display a broader mineral assemblage, including persistent aragonite and vaterite, whose stabilization appears related to curing conditions, CO_2 availability, and the coexistence of silicate–aluminate phases [57,60]. Moreover, clinker-derived phases such as C_3A and C_4AF (felite or ferrite) may hydrate into AFm compounds (hydrocalumite, carboaluminates, hydrotalcite) [5,16], further diversifying the mineralogical record of ancient binders.

With regard to $CaCO_3$ polymorphs, laboratory studies indicate that calcite is the dominant stable phase, but aragonite and vaterite can occasionally be detected in NHLs, their persistence being mainly dependent on carbonation conditions [57]. For instance, Parra-Fernández et al. [16] did not detect vaterite in the mineralogical composition of ten calcined NHL samples, while aragonite is detected, whereas such polymorphs were identified in the specimens analysed by Cantisani et al. [7]. These discrepancies highlight the role of production conditions and carbonation environment in stabilizing metastable phases.

Given these complex variables, we explored the composition and spatial distribution of historic natural hydraulic mortars in selected religious and historic buildings in Florence.

In Case A (Giotto's Bell Tower), calcite, aragonite, vaterite, and

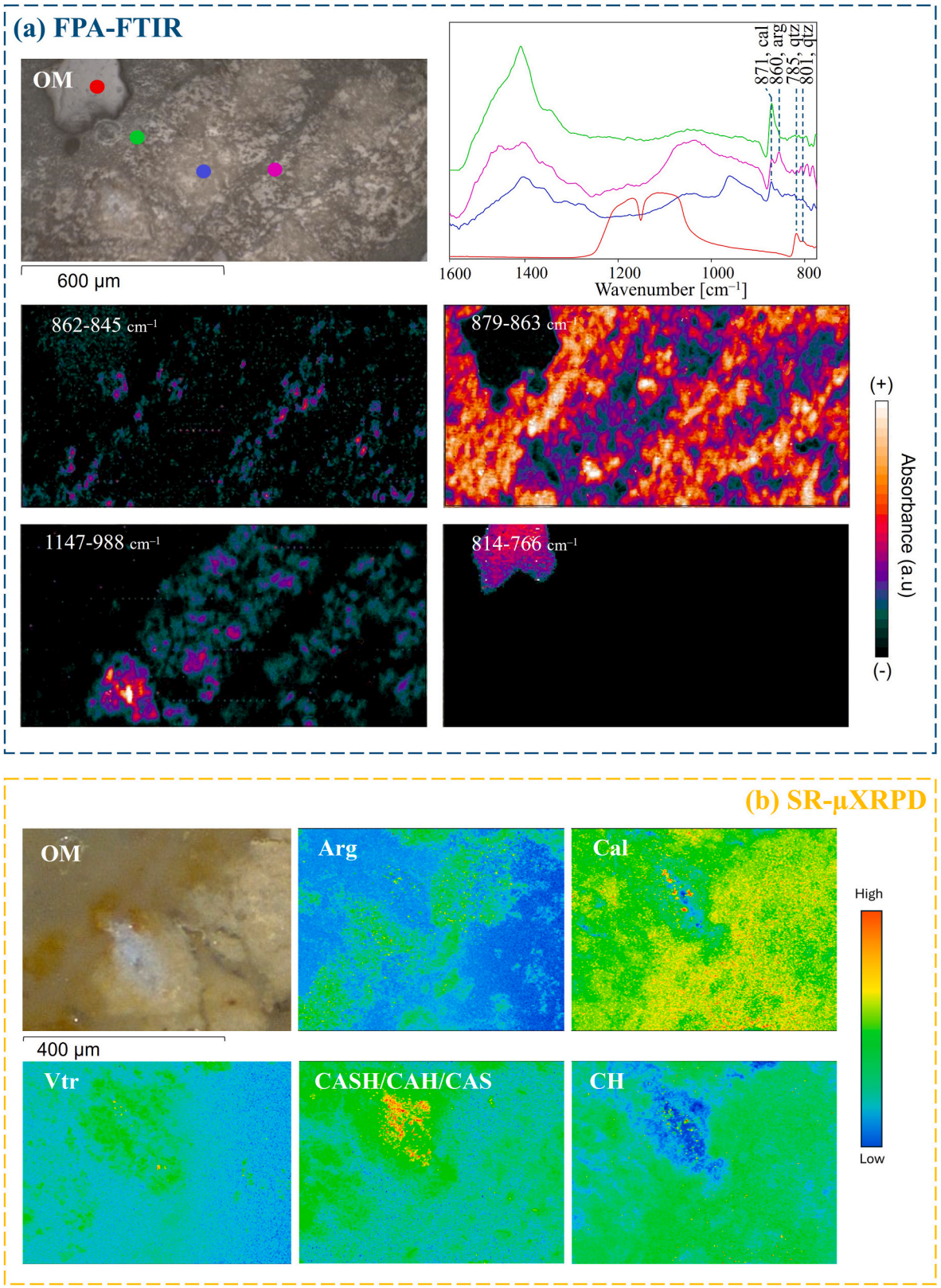

Fig. 5. Analysis of lump and binder with FPA-FTIR and SR-µXRPD. a) FPA-FTIR: Investigated area using OM (ROI ~1200 × 600 µm^2), point analysis, and absorbance spectra. Chemical distribution maps: aragonite (862–845 cm^{-1}), calcite/vaterite (879–863 cm^{-1}), silicate (1147–988 cm^{-1}) and quartz (814-766 cm^{-1}). b) SR-µXRPD: Investigated area using OM (ROI ~500 × 400 µm^2) and distribution maps: arg, cal, vtr, CASH/CAH/CAS, and portlandite (CH).

CASH phases were identified. The CASH phases were detected through SR-μXRPD analysis, which revealed the presence of gismondine. Gismondine, a hydrated calcium aluminate belonging to the AFm family, consistent with the hydration of C_3A and C_4AF in NHLs [60,61].

Amorphous and crystalline silicates were identified using FPA-FTIR. These phases were observed to be located in the same regions, particularly in association with vaterite. Relative distribution may indicate that silicates are the phases that stabilize vaterite and aragonite and slow the kinetics of conversion to calcite [17,18,21]. Vaterite is present in a concentrated area, the point where it is higher corresponds to a higher amount of CASH and is surrounded by calcite. The presence of CASH could be a factor that maintains the presence of vaterite as a stable phase. Aragonite is present along with CASH and is absent where the calcite and vaterite are mapped. This confirms the transformation sequence ACC-arg-vtr-cal [18,20].

In Case B (Trebbio Castle), the distribution of calcite, aragonite, and silicate phases was mapped. The distribution of calcite and aragonite is similar for both advanced techniques. Crystalline CASH or CAH phases were not identified through SR-μXRPD analysis but silicate phases were detected by FPA-FTIR. This indicates the presence of amorphous silicates. The absence of crystalline CASH/CAH suggests that hydration reactions were incomplete or dominated by amorphous silicates, consistent with literature on NHLs, where amorphous hydrates influence $CaCO_3$ polymorph stability and mortar mechanical properties [23,57]. It was observed that aragonite is generally absent in calcite-rich regions, and is mainly associated with the presence of amorphous silicates, concentrated in areas where calcite is less abundant.

In Case C (Medici Riccardi Palace), calcite, aragonite, vaterite, silicate phases were observed. Additionally, the detection of portlandite in SR-μXRPD analyses suggests that the carbonation process remains incomplete in certain areas. The CASH/CAH/CAS phases were detected through SR-μXRPD analysis, which results compatible with hydrocalumite and gehlenite peaks. Even in this case, the presence of vaterite corresponds to a higher amount of CASH and is surrounded by calcite and aragonite.

These findings are consistent with the expected hydration pathway of natural hydraulic binders: hydrocalumite represents a typical AFm phase from C_3A hydration in the presence of carbonate, while gehlenite (C_2AS) reflects high-temperature hydraulic phases [2,16,60,61]. Their coexistence with vaterite again highlights the stabilizing role of hydrated silicate–aluminate phases [60–62].

Another favourable factor for the crystallization of metastable polymorphs is the curing conditions of the mortar. The persistent presence of aragonite and vaterite may be related to the low CO_2 content, related also to environmental parameters [51,52]. $CaCO_3$ polymorphs can coexist in natural hydraulic mortar lumps and binder [2,7,16]. The final result of carbonation is calcite; however, aragonite and vaterite may also form and can be detected long after carbonation is complete. The reasons for finding these phases are complex. In this study, it was demonstrated that the presence of silicates can slow down the kinetic transformation process of calcium carbonate polymorphs.

The presence of portlandite is more common in mortar from core masonry (nucleus) sampled at greater depth in the walls.

The correlation between polymorph distribution, curing parameters, and the effects of trace elements provides a valuable interpretative key for both conservation and the design of compatible mortars. In particular, Mg, Fe, and Al can play a role in stabilizing metastable phases: Mg can hinder calcite growth and promote aragonite nucleation or ACC persistence, while Fe and Al favor the formation of ferric or aluminate hydrates that can interact with carbonate polymorphs [63]. These effects are especially evident in samples derived from marly raw materials, where MgO may also lead to the formation of magnesium silicate hydrates (MSH), recently investigated for their durability properties.

SEM-EDS analyses of the binder and lime lumps in our samples revealed a maximum MgO content of 1.4 wt% (see Table 1). Such low values fall below the thresholds reported in the literature as affecting the stability of $CaCO_3$ polymorphs or promoting the formation of magnesium silicate hydrates (MSH) [63,64]. Therefore, magnesium can be excluded as a controlling factor in our case studies.

These observations highlight the complexity of the chemical and mineralogical transformations involved and the importance of advanced analytical methods in their interpretation. Similarly, the microtexture and particle size, and their aggregation influence the persistence of certain phases in the mortar composition. Although particle sizes have been described in the literature [16], they can be variable and depend on preceding production processes [65].

The integration of these processes—calcination, slaking, and hardening—offers a comprehensive interpretative framework for explaining the variability of $CaCO_3$ polymorph distribution and the occurrence of amorphous and crystalline CASH/CAH phases in archaeological mortars.

This explains the differences between archaeological samples and laboratory/commercial samples, which undergo more homogeneous mixture production. When comparing our archaeological samples with the laboratory-produced NHLs described by Parra-Fernández et al. [16], clear differences emerge: the ancient mortars exhibit a broader polymorph assemblage, including metastable phases such as vaterite that are absent or short-lived in laboratory mortars. Moreover, our SR-μXRPD maps show the coexistence of hydraulic phases (CSH/CASH) and carbonates in the same micro-domains, suggesting simultaneous carbonation–hydration processes, whose development is difficult to ascertain. This points to a more complex reaction pathway in archaeological materials, likely influenced by variable kiln conditions, heterogeneous raw material chemistry, and fluctuating exposure to CO_2 and moisture over centuries.

5. Conclusion

To investigate the distribution of calcium carbonate polymorphs and the amorphous and crystalline silicate phases commonly found in hydraulic mortars, samples of historical Florentine mortars, traditionally produced with natural hydraulic binders, were selected and analysed.

A preliminary characterization of the mortar samples was performed: powders were collected and analysed using conventional techniques such as XRPD and ATR-FTIR. However, powder analyses alone are insufficient to fully understand the presence and distribution of different carbonate phases as well as crystalline and amorphous silicates within the same sample, due to the need for high lateral resolution. For this study, natural hydraulic mortars collected from Giotto's Bell Tower (Case A), Trebbio Castle (Case B) and Medici Riccardi Palace (Case C) in Florence were analysed through advanced techniques.

The same sample areas were analysed in thin sections with benchtop FPA-FTIR and at the European Synchrotron Radiation Facility (ESRF), with X-ray powder diffraction (SR-μXRPD) at the ID13 beamline, enabling 2D high lateral resolution mapping. These analyses allowed us to distinguish different chemical and mineralogical species based on their distinct spectral and diffraction patterns and to generate high-spatial-resolution maps of either crystalline (SR-μXRPD) or amorphous/crystalline (FPA-FTIR) compounds.

The study conducted using SR-μXRPD, FPA-FTIR and an appropriate sample preparation allowed for the in-depth evaluation of the distribution of $CaCO_3$ polymorphs and their formation, which is essential for understanding ancient production technologies and chemical transformations.

The complementarity of high-resolution imaging techniques such as FPA-FTIR and SR-μXRPD proved necessary to give answers to the controversial aspects of the formation of vaterite, aragonite, calcite and silicate phases in various ancient mortar samples.

A combination of advanced techniques can be applied to ancient and laboratory-prepared mortars to address key questions. For instance, we can examine the spatial relationship between the various hydraulic phases and calcium carbonate polymorphs present in hydraulic binders,

such as a mixture of air-hardening lime and pozzolans, hydraulic lime, formulated lime, natural cement, Portland cement, and white cement. These techniques can also be used to investigate microstructural heterogeneities within mortar texture, such as binder–aggregate rims.

Furthermore, understanding the mechanisms that have determined the durability of these materials can play an important role in the development of restoration materials and new sustainable mixtures.

CRediT authorship contribution statement

Sara Calandra: Writing – review & editing, Writing – original draft, Visualization, Software, Methodology, Investigation, Formal analysis, Data curation, Conceptualization. **Emma Cantisani:** Writing – review & editing, Writing – original draft, Validation, Supervision, Methodology, Investigation, Conceptualization. **Barbara Salvadori:** Writing – review & editing, Writing – original draft, Methodology, Investigation, Formal analysis.

Declaration of competing interest

The authors declare that they have no known competing financial interests or personal relationships that could have appeared to influence the work reported in this paper.

Acknowledgments

We thank Costanza Miliani for the access to the project HG-172 of Historical Materials BAG (Horizon 2020 Research and Innovation Programme of the European Union, Grant Agreement No. 870313, Streamline). We acknowledge the European Synchrotron Radiation Facility for provision of synchrotron radiation facilities and we would like to thank Manfred Burghammer, Alexey Melnikov and Liu Jiliang for assistance in using beamline ID13 (HG-172) and Marine Cotte for the valuable support during the beamtime at ID13. We sincerely acknowledge the TS Lab & Geoservices s. n.c (Cascina, Pisa, Italy) for preparation of the polished thin sections. Thanks are also due to Diego Sali (Bruker) for his invaluable support in the use of the FPA-FTIR LUMOS.

Data availability

Data will be made available on request.

References

[1] J.J. Hughes, K. van Balen, B. Bicer-Simsir, L. Binda, J. Elsen, R. van Hees, R. Veiga, Repair mortars for historic masonry: the role of mortar in masonry: an introduction to requirements for the design of repair mortars, Mater. Struct. 45 (2012) 1287–1294, https://doi.org/10.1617/s11527-012-98.

[2] A. Arizzi, G. Cultrone, Mortars and plasters – how to characterise hydraulic mortars, Archaeol. Anthropol. Sci. 13 (2021) 144, https://doi.org/10.1007/s12520-021-01404.

[3] E. Pecchioni, F. Fratini, E. Cantisani, Atlas of Ancient Mortars in Thin Section Under Optical Microscope, second ed., 2020. Nardini: Firenze, Italy.

[4] E. Cantisani, F. Fratini, E. Pecchioni, Optical and electronic microscope for minero-petrographic and microchemical studies of lime binders of ancient mortars, Minerals 12 (2022) 41, https://doi.org/10.3390/min1201004.

[5] G. Artioli, M. Secco, A. Addis, The Vitruvian legacy: mortars and binders before and after the Roman world, EMU Notes Miner 20 (2019) 151–202, https://doi.org/10.1180/EMU-notes.20.4.

[6] L.M. Seymour, J. Maragh, P. Sabatini, M. Di Tommaso, J.C. Weaver, A. Masic, Hot mixing: mechanistic insights into the durability of ancient Roman concrete, Sci. Adv. 9 (2023) eadd1602, https://doi.org/10.1126/sciadv.add1602.

[7] E. Cantisani, A. Falabella, F. Fratini, E. Pecchioni, S. Vettori, F. Antonelli, M. Giamello, M. Lezzerini, Production of the Roman cement in Italy: characterization of a raw material used in tuscany between 19th and 20th century and its comparison with a commercialized French stone material, Int. J. Architect. Herit. 12 (2018) 1038–1050, https://doi.org/10.1080/15583058.2018.1431730.

[8] N. Gadermayr, F. Pintér, J. Weber, Identification of 19th century Roman cements by the phase composition of clinker residues in historic mortars, in: E. Keats Webb (Ed.), 12th Int. Congr. Deterior. Conserv. Stone, 2012. New York.

[9] M. Lezzerini, M. Ramacciotti, F. Cantini, et al., Archaeometric study of natural hydraulic mortars: the case of the late roman villa dell'Oratorio (florence, Italy), archaeol, Anthropol. Sci. 9 (2017) 603–615, https://doi.org/10.1007/s12520-016-0404-2.

[10] A. Scala, F. Gabbrielli, M. Giamello, S. Mugnaini, Archaeometric analysis of building mortars used in the historic centre of Siena (Italy) between the 13th and 16th centuries, J. Archaeol. Sci. Rep. 35 (2021) 102790, https://doi.org/10.1016/j.jasrep.2021.102790.

[11] A. Moropoulou, A. Bakolas, K. Bisbikou, Characterization of ancient, Byzantine and later historic mortars by thermal and X-ray diffraction techniques, Thermochim. Acta 269–270 (1995) 779–795, https://doi.org/10.1016/0040-6031(95)02571-5.

[12] J.M. Maragh, J.C. Weaver, A. Masic, Large-scale micron-order 3D surface correlative chemical imaging of ancient Roman concrete, PLoS One 14 (2019) e0210710, https://doi.org/10.1371/journal.pone.0210710.

[13] S. Calandra, T. Salvatici, I. Centauro, E. Cantisani, C.A. Garzonio, The mortars of florence riverbanks: raw materials and technologies of lungarni historical masonry, Appl. Sci. 12 (2022) 5200, https://doi.org/10.3390/app12105200.

[14] M.M.N. Franceschini, G. Casa, S. Calandra, T. Ismaelli, C. Grifa, M. Mercurio, E. Cantisani, Raw materials and building technologies in the public buildings of pompeii after the earthquake of 62/63 CE: a diachronic analysis of mortars, Case Stud. Constr. Mater. 21 (2024) e03943, https://doi.org/10.1016/j.cscm.2024.e03943.

[15] Ö. Cizer, C. Rodriguez-Navarro, E. Ruiz-Agudo, J. Elsen, D. Van Gemert, K. Van Balen, Phase and morphology evolution of calcium carbonate precipitated by carbonation of hydrated lime, J. Mater. Sci. 47 (2012) 6151–6165, https://doi.org/10.1007/s10853-012-6535-7.

[16] C. Parra-Fernández, A. Arizzi, M. Secco, G. Cultrone, The manufacture of natural hydraulic limes: influence of raw materials' composition, calcination and slaking in the crystal-chemical properties of binders, Cement Concr. Res. 185 (2024) 107631, https://doi.org/10.1016/j.cemconres.2024.107631.

[17] T. Oghino, T. Suzuki, K. Sawada, The formation and transformation mechanism of calcium carbonate in water, Geochem. Cosmochim. Acta 51 (10) (1987) 2757–2767, https://doi.org/10.1016/0016-7037(87)90155-4.

[18] J. Zhu, J. Ding, P. Zhang, W. Dong, X. Zhao, M. Camaiti, X. Li, In-situ growth synthesis of nanolime/kaolin nanocomposite for strongly consolidating highly porous dinosaur fossil, Constr. Build. Mater. 300 (2021) 124312, https://doi.org/10.1016/j.conbuildmat.2021.124312.

[19] D.L. Whitney, B.W. Evans, Abbreviations for names of rock-forming minerals, Am. Mineral. 95 (1) (2010) 185–187, https://doi.org/10.2138/am.2010.3371.

[20] F. Liendo, M. Arduino, F.A. Deorsola, S. Bensaid, Factors controlling and influencing polymorphism, morphology and size of calcium carbonate synthesized through the carbonation route: a review, Powder Technol. 398 (2022) 117050, https://doi.org/10.1016/j.powtec.2021.117050.

[21] C. Rodriguez-Navarro, K. Kudłacz, Ö. Cizer, E. Ruiz-Agudo, Formation of amorphous calcium carbonate and its transformation into mesostructured calcite, CrystEngComm 17 (1) (2015) 58–72, https://doi.org/10.1039/C4CE01562B.

[22] L. Black, C. Breen, J. Yarwood, K. Garbev, P. Stemmermann, B. Gasharova, Structural features of C–S–H (I) and its carbonation in Air—a Raman spectroscopic study. Part II: carbonated phases, J. Am. Ceram. Soc. 90 (2007) 908–917, https://doi.org/10.1111/j.1551-2916.2006.01429.x.

[23] D. Frankeová, V. Koudelková, Influence of ageing conditions on the mineralogical micro-character of natural hydraulic lime mortars, Constr. Build. Mater. 264 (2020) 120205, https://doi.org/10.1016/j.conbuildmat.2020.120205.

[24] C. Fiori, M. Vandini, S. Prati, G. Chiavari, Vaterite in the mortars of a mosaic in the Saint Peter basilica, Vatican (Rome), J. Cult. Herit. 10 (2009) 248–257, https://doi.org/10.1016/j.culher.2008.07.011.

[25] L. Ventolà, M. Vendrell, P. Giraldez, L. Merino, Traditional organic additives improve lime mortars: new old materials for restoration and building natural stone fabrics, Constr. Build. Mater. 25 (2011) 3313–3318, https://doi.org/10.1016/j.conbuildmat.2011.03.020.

[26] D. Wang, C. Xiong, W. Li, J. Chang, Growth of calcium carbonate induced by accelerated carbonation of tricalcium silicate, ACS Sustainable Chem. Eng. 8 (2020) 14718–14731, https://doi.org/10.1021/acssuschemeng.0c02260.

[27] P. Lasch, M. Boese, A. Pacifico, M. Diem, FT-IR spectroscopic investigations of single cells on the subcellular level, Vib. Spectrosc. 28 (2002) 147–157, https://doi.org/10.1016/S0924-2031(01)00153-9.

[28] G. Della Ventura, F. Bellatreccia, A. Marcelli, et al., Application of micro-FTIR imaging in the Earth sciences, Anal. Bioanal. Chem. 397 (2010) 2039–2049, https://doi.org/10.1007/s00216-010-3811-8.

[29] S. Sotiropoulou, Z.E. Papliaka, L. Vaccari, Micro FTIR imaging for the investigation of deteriorated organic binders in wall painting stratigraphies of different techniques and periods, Microchem. J. 124 (2016) 559–567, https://doi.org/10.1016/j.microc.2015.10.002.

[30] E. Possenti, C. Colombo, M. Realini, et al., Insight into the effects of moisture and layer build-up on the formation of lead soaps using micro-ATR-FTIR spectroscopic imaging of complex painted stratigraphies, Anal. Bioanal. Chem. 413 (2021) 455–467, https://doi.org/10.1007/s00216-020-03016-6.

[31] G.-L. Liu, S.G. Kazarian, Recent advances and applications to cultural heritage using ATR-FTIR spectroscopy and ATR-FTIR spectroscopic imaging, Analyst 147 (2022) 1777–1797, https://doi.org/10.1039/D2AN00005A.

[32] M. Cotte, V. Gonzalez, F. Vanmeert, L. Monico, C. Dejoie, M. Burghammer, L. Huder, W. de Nolf, S. Fisher, I. Fazlic, C. Chauffeton, G. Wallez, N. Jiménez, F. Albert-Tortosa, N. Salvadó, E. Possenti, C. Colombo, M. Ghirardello, D. Comelli, E. Avranovich Clerici, R. Vivani, A. Romani, C. Costantino, K. Janssens, Y. Taniguchi, J. McCarthy, H. Reichert, J. Susini, The "historical materials BAG": a new facilitated access to synchrotron X-ray diffraction analyses for cultural heritage materials at the European synchrotron radiation facility, Molecules 27 (6) (2022) 1997, https://doi.org/10.3390/molecules27061997.

[33] M. Cotte, A. Genty-Vincent, K. Janssens, J. Susini, Applications of synchrotron X-ray nano-probes in the field of cultural heritage, C. R. Phys. 19 (2018) 575–588, https://doi.org/10.1016/j.crhy.2018.07.002.
[34] L. Bertrand, M. Cotte, M. Stampanoni, M. Thoury, F. Marone, S. Schöder, S. Development, And trends in synchrotron studies of ancient and historical materials, Phys. Rep. 519 (2012) 51–96.
[35] K. Janssens, M. Cotte, Using synchrotron radiation for characterization of cultural heritage materials, in: E. Jaeschke, S. Khan, J.R. Schneider, J.B. Hastings (Eds.), Synchrotron Light Sources and Free-Electron Lasers: Accelerator Physics, Instrumentation and Science Applications, Springer International Publishing, Cham, Switzerland, 2019, pp. 1–27.
[36] E. Cantisani, S. Calandra, S. Barone, S. Caciagli, M. Fedi, C.A. Garzonio, L. Liccioli, B. Salvadori, T. Salvatici, S. Vettori, The mortars of Giotto's bell tower (Florence, Italy): raw materials and technologies, Constr. Build. Mater. 267 (2021) 120801, https://doi.org/10.1016/j.conbuildmat.2020.120801.
[37] S. Calandra, E. Cantisani, C. Conti, B. Salvadori, S. Barone, L. Liccioli, M. Fedi, T. Salvatici, A. Arrighetti, F. Fratini, C.A. Garzonio, A new multi-analytical procedure for radiocarbon dating of historical mortars, Sci. Rep. 14 (2024) 19979, https://doi.org/10.1038/s41598-024-70763-2.
[38] E. Possenti, C. Miliani, M. Cotte, M. Realini, C. Colombo, SR-based μXRD-μXRF 2D mapping to study Mg-rich historical frescoes treated with inorganic conservation treatments, Analyst (2025), https://doi.org/10.1039/D4AN01548G.
[39] J. Vandeperre, F. Giuliani, S.J. Lloyd, W.J. Clegg, The hardness of silicon and germanium, Acta Mater. 55 (18) (2007) 6307–6315, https://doi.org/10.1016/j.actamat.2007.07.036.
[40] B.Z. Dilnesa, B. Lothenbach, G. Renaudin, A. Wichser, D. Kulik, Synthesis and characterization of hydrogarnet $Ca_3(Al_xFe_{1-x})_2(SiO_4)_y(OH)_4(3-y)$, Cement Concr. Res. 59 (2014) 96–111, https://doi.org/10.1016/j.cemconres.2014.02.001.
[41] N.V. Vagenas, A. Gatsouli, C.G. Kontoyannis, Quantitative analysis of synthetic calcium carbonate polymorphs using FT-IR spectroscopy, Talanta 59 (4) (2003) 831–836, https://doi.org/10.1016/S0039-9140(02)00638-0.
[42] V.C. Farmer, The infrared spectra of minerals, Mineralogical Society Monograph 4 (1974) 331–363. Mineralogical Society, London.
[43] B.J. Saikia, G. Parthasarathy, N.C. Sarmah, Fourier transform infrared spectroscopic estimation of crystallinity in SiO_2 based rocks, Bull. Mater. Sci. 31 (2008) 775–779, https://doi.org/10.1007/s12034-008-0123-0.
[44] R. Ellerbrock, M. Stein, J. Schaller, Comparing amorphous silica, short-range-ordered silicates and silicic acid species by FTIR, Sci. Rep. 12 (1) (2022) 11708, https://doi.org/10.1038/s41598-022-15882-4.
[45] L.Z. Lakshtanov, S.L.S. Stipp, Interaction between dissolved silica and calcium carbonate: 1. Spontaneous precipitation of calcium carbonate in the presence of dissolved silica, Geochem. Cosmochim. Acta 74 (9) (2010) 2655–2664, https://doi.org/10.1016/j.gca.2010.02.009.
[46] M.U. Okoronkwo, S.K. Mondal, B. Wang, H. Ma, A. Kumar, Formation and stability of gismondine-type zeolite in cementitious systems, J. Am. Ceram. Soc. 104 (3) (2021) 1513–1525, https://doi.org/10.1111/jace.17572.
[47] W. Ma, Y. Yi, M. Fang, C. Li, J. Li, W. Liu, Study on the synthesis mechanism of sodalite, gismondine, and zeolite-P1 zeolite materials from ladle furnace slag and fly ash, Sci. Rep. 13 (2023) 3232, https://doi.org/10.1038/s41598-023-30282-y.
[48] J. Bertaux, F. Fröhlich, P. Ildefonse, Multicomponent analysis of FTIR spectra: quantification of amorphous and crystallized mineral phases in synthetic and natural sediments, J. Sediment. Res. 68 (3) (1998) 440–447, https://doi.org/10.2110/jsr.68.440.
[49] J. Partyka, M. Leśniak, Raman and infrared spectroscopy study on structure and microstructure of glass–ceramic materials from SiO_2–Al_2O_3–Na_2O–K_2O–CaO system modified by variable molar ratio of SiO_2/Al_2O_3, Spectrochim. Acta Mol. Biomol. Spectrosc. 152 (2016) 82–91, https://doi.org/10.1016/j.saa.2015.07.045.
[50] H. Chen, G. Huang, M. Han, F. Gan, Structure and raman spectra of glasses containing several glass-forming oxides and no glass-modifying oxide, J. Non-Cryst. Solids 80 (1–3) (1986) 152–159, https://doi.org/10.1016/0022-3093(86)90389-3.
[51] H. Klöppel, A. Fliedner, W. Kordel, Behaviour and ecotoxicology of aluminum in soils and Waters—a review of the scientific literature, Chemosphere 35 (1997) 353–363, https://doi.org/10.1016/S0045-6535(97)00148-3.
[52] A.B. Cerato, Mineralogical study of davis mine, rowe, Massachusetts, M.S. project report, in: Department of Geosciences, University of Massachusetts-Amherst, 2003, p. 140.
[53] P. Kozlovcev, R. Přikryl, Compositional characteristics and experimental burning of selected lower Palaeozoic limestones from the prague basin (Barrandian area, Czech Republic) suitable for the production of natural hydraulic lime, Bull. Eng. Geol. Environ. 76 (2017) 21–37, https://doi.org/10.1007/s10064-016-0882-6.
[54] M. Foldvari, Handbook of thermogravimetric system of minerals and its use in geological practice, in: Occasional Papers of the Geological Institute of Hungary, vol.213, Geological Institute of Hungary, Budapest, 2011.
[55] J. Elsen, M.D. Jackson, E. Ruiz-Agudo, Historic concrete science: opus caementicium to "natural cements", Elements 18 (5) (2022) 301–307, https://doi.org/10.2138/gselements.18.5.301.
[56] I.M. Ritchie, X. Bing-An, The kinetics of lime slaking, Hydrometallurgy 23 (2–3) (1990) 377–396, https://doi.org/10.1016/0304-386X(90)90018-W.
[57] A. Arizzi, C. Parra-Fernandez, A comprehensive review of the manufacturing process and properties of natural hydraulic limes, Mater. Struct. 58 (4) (2025) 152, https://doi.org/10.1617/s11527-025-02364-8.
[58] J.H. Potgieter, S.S. Potgieter, S.J. Moja, A. Mulaba-Bafubiandi, An empirical study of factors influencing lime slaking, part I: production and storage conditions, Miner. Eng. 15 (3) (2002) 201–203, https://doi.org/10.1016/S0892-6875(02)00008-0.
[59] F. Massazza, Properties and applications of natural pozzolanas, in: J. Bensted, P. Barnes (Eds.), Structure and Performance of Cements, second ed., Spon Press, Taylor & Francis Group, New Fetter Lane, 2002, pp. 326–352.
[60] R.S. Boynton, Chemistry and Technology of Lime and Limestone, second ed., John Wiley & Sons Inc., New York, 1980.
[61] J. Elsen, G. Mertens, R. Snellings, Portland cement and other calcareous hydraulic binders: history, production and mineralogy, in: G.E. Christidis (Ed.), Advances in the Characterization of Industrial Minerals, vol. 9, European Mineralogical Union Notes in Mineralogy, London, 2010, pp. 441–479, https://doi.org/10.1180/EMU-notes.9.11.
[62] T. Matschei, B. Lothenbach, F.P. Glasser, The role of calcium carbonate in cement hydration, Cement Concr. Res. 37 (4) (2007) 551–558, https://doi.org/10.1016/j.cemconres.2006.10.013.
[63] E. Loste, R.M. Wilson, R. Seshadri, F.C. Meldrum, The role of magnesium in stabilising amorphous calcium carbonate and controlling calcite morphologies, J. Cryst. Growth 254 (1–2) (2003) 206–218, https://doi.org/10.1016/S0022-0248(03)01153-9.
[64] J. Aufort, R. Demichelis, Magnesium impurities decide the structure of calcium carbonate hemihydrate, Cryst. Growth Des. 20 (12) (2020) 8028–8038, https://doi.org/10.1021/acs.cgd.0c01025.
[65] C. Pesce, M.C. Godina, A. Henry, G.L. Pesce, Effects of steam-slaking on the characteristics of lime from three different UK manufacturers, in: J.I. Escalante-Garcia, P. Castro Borges, A. Duran-Herrera (Eds.), Proceedings of the 75th RILEM Annual Week 2021 (RW 2021), RILEM Bookseries, vol. 40, Springer, Cham, 2023, pp. 807–815, https://doi.org/10.1007/978-3-031-21735-7_82.